

Cite this article as: Xu Yang, Liu Gaoshang, Liu Chengbao, et al. Facile Synthesis of Porous Biocarbon Decorated with MnO-Co Nanocrystals for High-Capacitance Electrodes[J]. Rare Metal Materials and Engineering, 2024, 53(07): 1855-1862. DOI: 10.12442/j.issn.1002-185X.E20230043.

ARTICLE

# Facile Synthesis of Porous Biocarbon Decorated with MnO-Co Nanocrystals for High-Capacitance Electrodes

Xu Yang<sup>1,2</sup>, Liu Gaoshang<sup>1,2</sup>, Liu Chengbao<sup>1,2,3</sup>, Zheng Leizhi<sup>1,2,3</sup>, Chen Feng<sup>1,2,3</sup>, Qian Junchao<sup>1,2,3</sup>, Qiu Yongbin<sup>4</sup>, Meng Xianrong<sup>5</sup>, Chen Zhigang<sup>1,2,3</sup>

<sup>1</sup> Jiangsu Key Laboratory for Environment Functional Materials, Suzhou University of Science and Technology, Suzhou 215009, China; <sup>2</sup> School of Materials Science and Engineering, Suzhou University of Science and Technology, Suzhou 215009, China; <sup>3</sup> Jiangsu Collaborative Innovation Center of Technology and Material for Water Treatment, Suzhou University of Science and Technology, Suzhou 215009, China; <sup>4</sup> Jiangsu Province Ceramics Research Institute Co., Ltd, Yixing 214221, China; <sup>5</sup> Suzhou Institute of Environmental Science, Suzhou 215007, China

**Abstract:** With the rapid depletion of fossil fuels and a series of environmental problems, it is urgent to develop and to utilize new electrochemical energy storage devices, and the design, preparation and optimization of electrode materials are key factors to determine the performance of supercapacitors. Hydrothermal method was used to convert hollyhock stalks into porous carbon matrix with MnO and Co nanocrystals anchored on it. Results show that the prepared biocarbon has porous structure and good electron transport properties, and the nanocrystal MnO-Co on it has high capacitance. Due to the unique nanostructure of carbon skeleton and large specific surface area ( $345.9 \text{ m}^2 \cdot \text{g}^{-1}$ ), MnO-Co nanocrystal/porous carbon shows excellent electrochemical capacitance ( $146 \text{ F} \cdot \text{g}^{-1}$  at  $1 \text{ A} \cdot \text{g}^{-1}$ ) and cycle stability. After 1000 cycles, the specific capacity still remains 99.4%.

**Key words:** MnO-Co nanocrystals; energy storage; electrode material; porous biocarbon

With the increasing demand for energy, human are facing the dilemma of fossil fuels depletion and serious environmental pollution problems caused by burning them<sup>[1]</sup>. Therefore, new energy such as solar energy, wind energy and biomass energy are introduced into the energy system. However, some of the new energy cannot be used efficiently because of its poor consistency property. So the energy storage devices such as supercapacitors have gained great interests, especially for electric vehicles and electronic products<sup>[2-4]</sup>. In fact, the large-scale commercial application of supercapacitors depends largely on the development of electrode materials. Nature endows biomass with accessibility, low cost and special microstructures. In particular, biomass carbon with the hierarchical porous structure can be obtained from agricultural or domestic waste. Therefore, as an important renewable energy material, biomass carbon and its composites have attracted much attention for

supercapacitors<sup>[5-8]</sup>.

In recent years, a variety of biomass has been extensively studied as a precursor to prepare biomass carbon and its composites for supercapacitors use, such as fruit<sup>[9]</sup>, stems<sup>[10]</sup> and fungi<sup>[11]</sup>. The results show that the hierarchical structure of biomass carbon promotes electrolyte penetration and reduces ion transport pathways. In addition, Nitrogen atoms in biomass can induce heteroatom doping of carbon materials, which may endow it higher conductivity and more active sites<sup>[12]</sup>. Therefore, due to various layered structures, environmental protection functions, natural abundance and simple preparation methods, biomass carbon and its composites have been considered as extremely competitive supercapacitor and battery materials. For example, Liu et al<sup>[5]</sup> has produced robust 3D porous carbon from low-cost biomass through high-temperature carbonization and subsequent KOH activation, and found that the electrode material exhibits high

Received date: October 11, 2023

Foundation item: Natural Science Foundation of Jiangsu Province (BK20180103, BK20180971); Science and Technology Development Project of Suzhou (SS202036)

Corresponding author: Liu Chengbao, Ph. D., Associate Professor, Jiangsu Key Laboratory for Environment Functional Materials, Suzhou University of Science and Technology, Suzhou 215009, P. R. China, Tel: 0086-512-68242750, E-mail: Lcb@mail.usts.edu.cn

Copyright © 2024, Northwest Institute for Nonferrous Metal Research. Published by Science Press. All rights reserved.

volumetric capacitance of  $476 \text{ F}\cdot\text{cm}^{-3}$  in 6 mol/L KOH electrolyte and its energy storage efficiency can still be maintained at 91% after 10000 cycles.

In fact, metallic compound<sup>[13-16]</sup> are usually introduced due to its pseudocapacitance behavior to prepare mixed electrode materials with high specific capacitance. Among the transition metals, Mn has the largest number of oxides, most of which have a special tunnel structure that can undergo bulk redox reactions. The higher theoretical capacitance, wider potential window and higher natural abundance make  $\text{MnO}_x$ <sup>[17-18]</sup> species the main electrode material for energy storage applications. Cobalt oxide ( $\text{Co}_3\text{O}_4$ ) has a high theoretical capacity ( $3560 \text{ F}\cdot\text{g}^{-1}$ ), and exhibits excellent electrochemical performance<sup>[19]</sup>. However, it is still challenging to manufacture supercapacitors based on  $\text{Co}_3\text{O}_4$  with high specific capacitance, because the specific capacitance observed in many cases is much lower than the theoretical value<sup>[20-21]</sup>. When the  $\text{Co}_3\text{O}_4$  composite material undergoes a phase change with respect to the electrolyte medium, it may show a sharp decrease in cycle performance over a longer period of use. This is due to the continuous change of the oxidation state from  $\text{Co}^{2+}/\text{Co}^{3+}$  to  $\text{Co}^{3+}/\text{Co}^{4+}$ <sup>[22]</sup>, and the transfer of charge causes an increase in resistance and a significant decrease in cycle performance. Therefore, the uneven distribution of metal oxides and structural collapse are two difficult problems that restrict the development of biomass carbon/metal oxide hybrid supercapacitor electrodes.

In this work, MnO and oxide-free Co metal was embedded into the biocarbon matrix to mitigate the problems of phase transition and the structural collapse caused by the phase transition. Cobalt metal also plays an important role in preventing crystal caking, and it interacts with MnO during the crystallization process to prevent crystals from caking to form smaller nanoparticles<sup>[23-24]</sup>. Through the water-absorbing and water-retaining capacity of hollyhock stems, the dried stems can absorb the required metal salt solution. Finally, a uniformly distributed MnO-Co/biocarbon composite was prepared by calcination. The morphology, pore structure and supercapacitor performance of MnO-Co/biocarbon composite were tested, and the electrochemical storage mechanism was proposed.

## 1 Experiment

### 1.1 Chemicals and materials

Manganese acetate tetrahydrate and cobalt nitrate hexahydrate were of analytical grade and used without further purification. They were purchased from Aladdin Industrial Corporation (Shanghai, China). Hollyhock stalks were collected in campus and used after a series of treatments.

### 1.2 Template preprocessing

The green epidermis of the hollyhock stalks was stripped away by means of peeling, leaving only the white part of the interior. The long stems were sterilized in an ultra-clean bench (sterilization time: 15 min). Then, the long stems were cut into small segments with a basically consistent length of 4 cm to

5 cm. The samples were rinsed 3 or 4 times with deionized water to remove impurities from the stalks themselves during the stripping process. The preprocessing solution was prepared as follows: deionized water and absolute ethanol ( $\text{C}_2\text{H}_5\text{OH}$ ) were introduced into the prepared beaker in a volume ratio of 1:1, and then the pre-formulated 0.1 mol/L hydrochloric acid (HCl) was dropwise added to adjust the pH value as 2–3. An appropriate amount of hollyhock stalks aforementioned were introduced. The beaker with preprocessing solution and hollyhock stalks was sealed by transparent plastic wrap and the stalks were fully immersed in the solution for 3 d.

The hollyhock stalks obtained were rinsed by deionized water for several times, and then the preprocessing process was repeated for another 3 d. Then, after rinsed by distilled water several times to neutral state to avoid residue of ethanol or hydrochloric acid, the pre-template samples were produced. Finally, the pre-template samples were put into a vacuum drying box at  $40^\circ\text{C}$  for about 24 h, and the stem template material was obtained.

### 1.3 Preparation of MnO-Co/biocarbon

A certain amount of  $\text{Mn}(\text{CH}_3\text{COO})_2\cdot 4\text{H}_2\text{O}$  and  $\text{Co}(\text{NO}_3)_2\cdot 6\text{H}_2\text{O}$  were calculated and weighed according to the molar ratio of Mn:Co as 4:1, 2:1 and 1:1. Then, the weighed metal salt was stirred thoroughly with deionized water until it was completely dissolved into the transparent solution. Hollyhock stems were pretreated with the same quality of the template and divided into three parts. Then, the stems sunk in the completely dissolved metal salt solution for 24 h until the mixture reached an osmotic pressure equilibrium. The soaked stalks were transferred to a polytetrafluoroethylene lining with 50 mL ethanol and reacted at  $160^\circ\text{C}$  for 6 h. After cooling to room temperature, the stems were put in a porcelain boat and dried at  $60^\circ\text{C}$  in a vacuum drying oven. Finally, the porcelain boat was put into a tube furnace charged with  $\text{N}_2$  at a heating rate of  $5^\circ\text{C}\cdot\text{min}^{-1}$  to  $800^\circ\text{C}$  and held for 4 h, and the MnO-Co/biocarbon composite material was prepared.

### 1.4 Material characterization

Morphology and structure of MnO-Co/biocarbon composite material were identified by JOEL JEM-2100F transmission microscope (TEM) equipped with energy dispersive spectroscope (Bruker EDS X Flash 6T|60). Phase of the MnO-Co/biocarbon composite material was collected by X-ray diffraction (XRD, D8 Advanced XRD, Bruker, Germany, wavelength =  $0.15148 \text{ nm}$ ) with Cu  $\text{K}\alpha$  radiation within the  $2\theta$  range of  $10^\circ$ – $80^\circ$ . A micromeritics ASAP 2020 apparatus was used to measure the surface areas of as-prepared sample at liquid nitrogen temperature after the sample was degassed in a vacuum at  $200^\circ\text{C}$  for 2 h. X-ray photoelectron spectroscopy (XPS, Thermo ESCALAB 250XI) was used to analyze the surface components of the MnO-Co/biocarbon composite material. All binding energies referred to the C 1s peak at  $284.8 \text{ eV}$ .

### 1.5 Electrochemical measurements

In the three-electrode system, the saturated calomel

electrode (SCE) was used as a reference electrode, the platinum electrode was used as a counter electrode, and the prepared material was used as a working electrode. The electrolyte was 0.5 mol/L  $\text{Na}_2\text{SO}_4$  aqueous solution. The electrochemical performance was estimated by the cyclic voltammetry (CV), galvanostatic charge-discharge (GCD), and AC impedance tests.

## 2 Results and Discussion

The thermodynamic decomposition process of marshmallow stalk impregnated with Mn and Co metal salt solution was analyzed by thermogravimetry (TG) method. Fig.1 shows the TG curve of marshmallow stem after impregnation. It can be seen that the mass loss of the sample can be divided into three stages. The first stage is from room temperature to 100 °C, which is mainly the evaporation process of physically adsorbed water. In the second stage (100–360 °C), the sample mass decreases significantly, mainly due to the carbonization of the stem template and the decomposition of metal salts. In the third stage, mass loss is slow from 360 °C to 800 °C, and tends to stabilize at 800 °C. In conclusion, 800 °C was used to carbonize the pretreated biological template.

Fig. 2 shows XRD patterns of MnO-Co/biocarbon composites. It can be seen that the peak intensity and position are well matched with Co phase (JCPDS 15-0806) and MnO phase (JCPDS 75-1090). The diffraction peaks at 44.2°, 51.5° and 75.8° correspond to the (111), (200) and (220) phases of Co, respectively. The diffraction peaks at 34.8°, 40.3°, 58.6°, 70.0° and 73.7° are assigned to the (111), (200), (220), (311) and (222) phases of MnO, respectively. There is no obvious

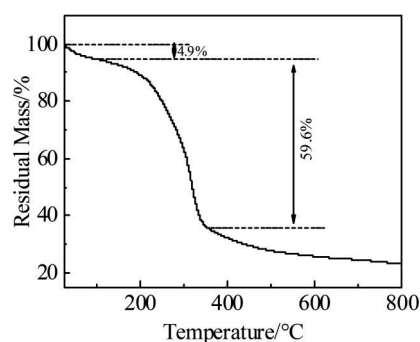


Fig.1 TG curve after immersion in Mn and Co metal salt solution

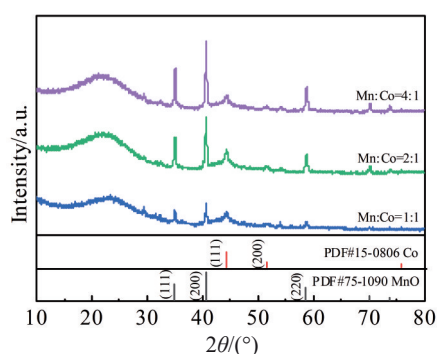


Fig.2 XRD patterns of samples with different Mn:Co ratios

impurity peak, indicating that the particles loaded on the C template are MnO and Co. Comparing XRD patterns of samples with different proportions, it can be seen that the sample with Mn:Co=4:1 has the strongest diffraction peak, higher peak strength and narrower half peak width, indicating that the particle crystallinity is better. It can be speculated that it is easy to agglomerate due to the high content of manganese. The main diffraction peak intensity of Co in the sample with Mn:Co=1:1 is relatively weak, indicating that the crystallinity of nanoparticles is not good. The crystallinity of the sample with Mn:Co=2:1 is moderate and the half peak width is wider.

Fig. 3a is the SEM image of manganese and cobalt nanocrystals under hydrothermal conditions. It can be seen that manganese oxide is prone to agglomerate and to form large particles without spatial limitation of carbon template. Fig. 3b – 3d are SEM images of different proportions of manganese and cobalt under the biochar template. It can be seen that the particles are uniformly distributed on the biochar material, indicating that the existence of template carbon plays a good restrictive role. The large specific surface area of carbon makes it conducive to contact with electrolyte, which limits the domain of particles and effectively prevents particle agglomeration. From Fig.3b–3d, it can be seen that the size of the composite material gradually increases with the increase in Mn content, because the increase in Mn content leads to insufficient Co metal to interact with MnO in the crystallization process, resulting in crystal growth and an increase in particle size. The larger the particle size, the easier the partial agglomeration.

The TEM images of MnO-Co/biocarbon at different magnifications are shown in Fig.4a–4c. From Fig.4a, it can be observed that the particles are uniformly distributed on the carbon substrate, the particles are fine, and the carbon layer is thin. The inset in Fig.4a shows the particle size distribution of the material, and it can be seen that the main size of the prepared nanocrystals is 15–20 nm. The carbon layer is further enlarged. The particle size is relatively uniform without obvious agglomeration in Fig.4b. The particle size is 10–25 nm, which is basically consistent with the statistical particle size shown in the inset of Fig.4a. Fig.4c clearly shows lattice fringes of the (111) crystal plane of MnO nanoparticles, with a crystal plane spacing of 0.25 nm. The lattice fringes of most of the particles are not clear, and it is presumed that the particles are embedded in the carbon layer, resulting in unclear lattice lines. This phenomenon is attributed to the porous structure, in which nanoparticles are embedded, avoiding the agglomeration phenomenon. Fig.4d is the energy spectrum of this region. It can be seen that the sample contains C, Mn, Co and O elements, and no other elements exist, suggesting that the material is relatively pure.

XPS is used to further analyze the surface chemical composition and valence state of elements in MnO-Co/biocarbon composites, as shown in Fig. 5. Fig.5a shows the XPS full spectrum of MnO-Co/biocarbon composites, indicating that the prepared samples are mainly composed of

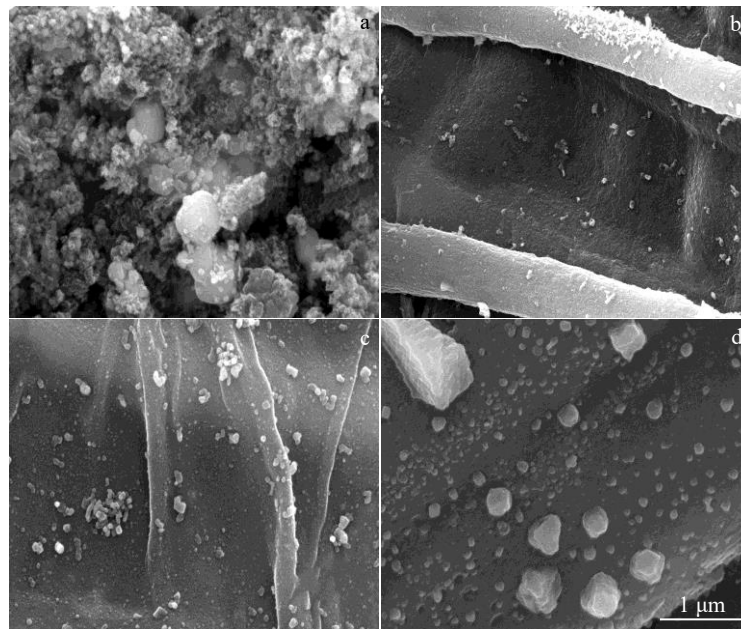


Fig.3 SEM image of Mn and Co nanocrystal (Mn:Co=1:1) (a); SEM images of biocarbon-loaded nanocrystals with Mn:Co ratios of 1:1 (b), 2:1 (c), and 4:1 (d)

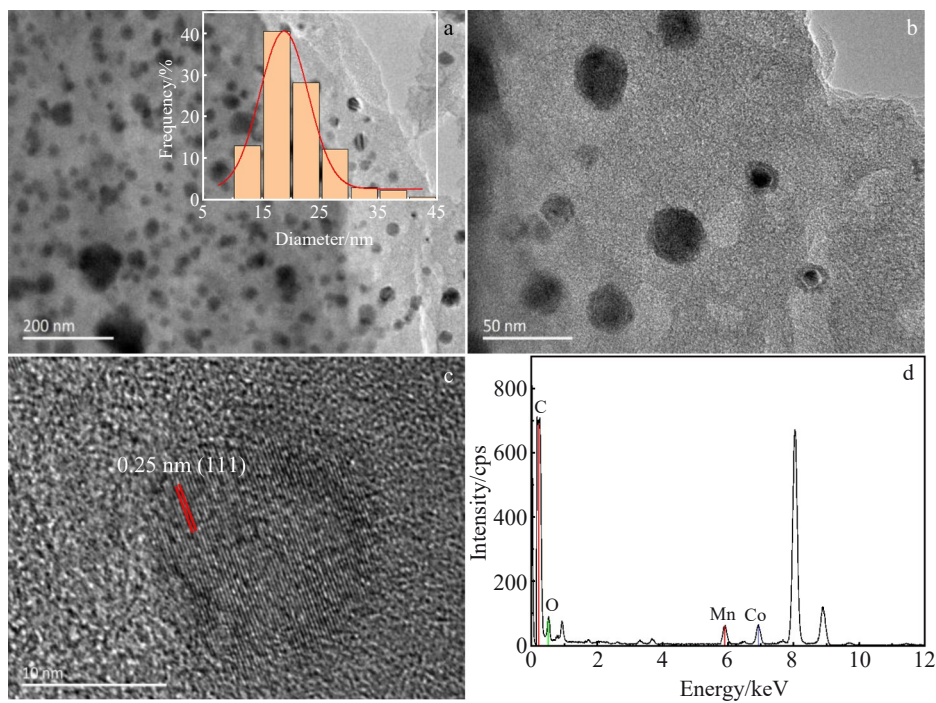


Fig.4 TEM images of MnO-Co/biocarbon at different magnifications (a-c) and EDS spectrum corresponding to Fig.4c (d)

C, O, Mn and Co elements. At the same time, there is no obvious impurity peak, indicating that the elements in the material are relatively pure. As shown in Fig. 5b, the characteristic peaks corresponding to Co just conform to  $2p_{3/2}$  and  $2p_{1/2}$ , indicating that Co element mainly appears in the form of metal phase in the material<sup>[25]</sup>. The high-resolution spectra of O 1s in Fig. 5c can be simulated into two peaks, corresponding to Mn-O bond with binding energy of 529.3 eV

and C-O bond formed by surface amorphous carbon with binding energy of 531.4 eV. Fig. 5d shows the high-resolution C 1s spectra, which can be divided into three peaks with binding energies of 283.9, 285.03 and 288.8 eV. The peak at the binding energy of 283.9 eV is attributed to the C-C coordination of surface amorphous carbon. Fig. 5e shows the high-resolution Mn 2p spectra, in which two distinct peaks at 640.6 and 652.6 eV can be ascribed to Mn  $2p_{1/2}$  and Mn  $2p_{3/2}$

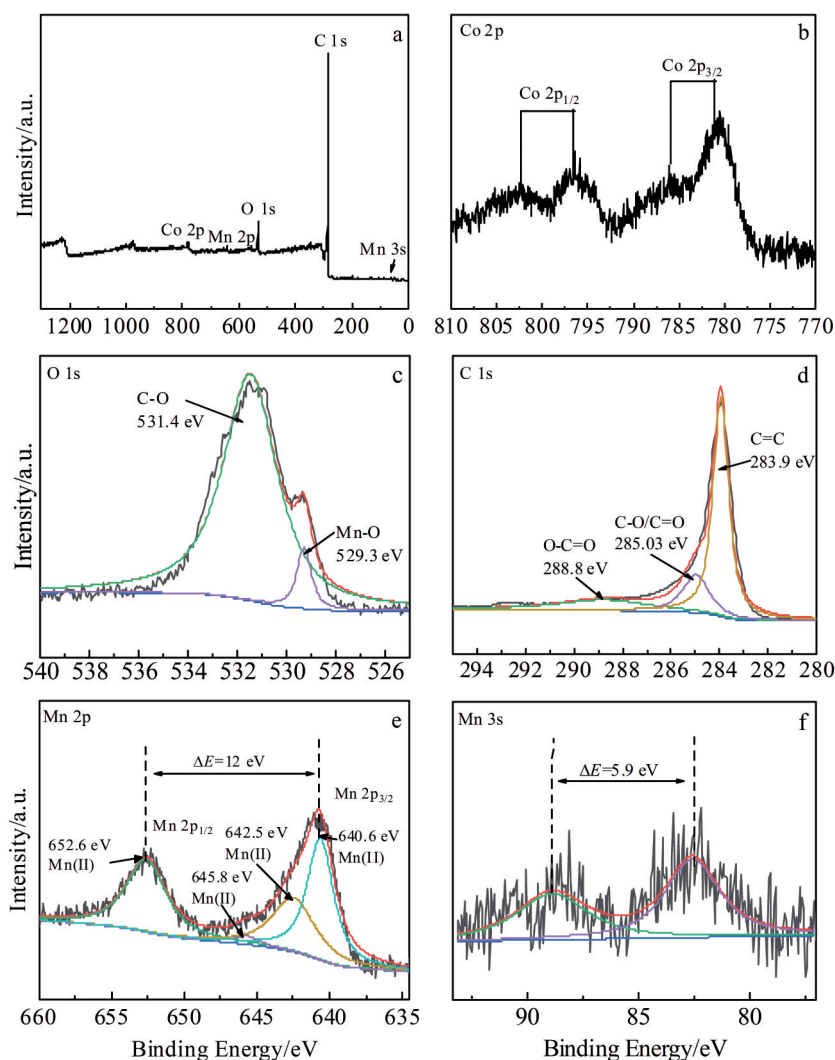


Fig.5 XPS full spectrum (a) and fine spectra of each element (b–f) of MnO-Co/biocarbon

of Mn(II) state, which pass through the two characteristic peaks with  $\Delta E=12$  eV<sup>[26–27]</sup>. Peaks at 642.5 and 645.8 eV are ascribed as the shake-up peak and the satellite peak, respectively<sup>[28–29]</sup>. Fig.5e shows the high-resolution Mn 2p with spectra with two characteristic peaks ( $\Delta E=5.9$  eV). It can be concluded that Mn exists in the form of MnO<sup>[30]</sup>, which is consistent with the results of XRD.

The N<sub>2</sub> adsorption-desorption isotherm in Fig. 6a shows a typical type I isotherm and has a unique H<sub>4</sub> hysteresis loop, which is a typical shape of materials containing a large number of micropores<sup>[31]</sup>. In the region of low relative pressure, the gas adsorption capacity increases rapidly. This is mainly due to micropore filling. The subsequent approximate horizontal platform shows that the micropores have been filled. The relative pressure  $P/P_0$  has H4 type hysteresis loop from 0.42<sup>[31]</sup>, which is due to the existence of long and narrow cracks and pores in the accumulation of sheet samples, resulting in capillary condensation and the non-coincidence of adsorption and desorption isotherms and hysteresis loop. The BET specific surface area ( $S_{\text{BET}}$ ) is calculated as 345.9 m<sup>2</sup>·g<sup>-1</sup>. Fig.6c shows a typical capillary pressure curve. The mercury

injection curve is hillside-type, which means that mercury first penetrates into the large pores and then into the smaller pores. The general model of N<sub>2</sub> adsorption method covers the pores with 5–50 nm in diameter. The ultra-low pressure model of nitrogen adsorption method covers the pores with 0.5–5 nm in diameter, while the pore size range covered by MIP is 50–100 μm. Through the pore size distribution diagrams (Fig.6b and 6d), it can be seen that the sample has plenty of macropores, slit mesopores and micropores. Plentiful pore structure and large specific surface area are conducive to high energy storage density, rapid charge and discharge performance and long service life.

Fig. 7a shows the CV curves of different reference samples tested at a scanning rate of 100 mV·s<sup>-1</sup> in three electrode mode. The shape of the CV curves deviates from the rectangular shape because there are redox peaks in the CV curve. It is reported that during the initial electrochemical activation, MnO nanoparticles can be oxidized to Mn<sub>3</sub>O<sub>4</sub> and MnO<sub>2</sub>, and then work based on the charge storage mechanism of Mn<sub>3</sub>O<sub>4</sub> and MnO<sub>2</sub>, corresponding to the redox of the CV curve in Fig. 7a<sup>[32–34]</sup>. These results suggest the coexistence of

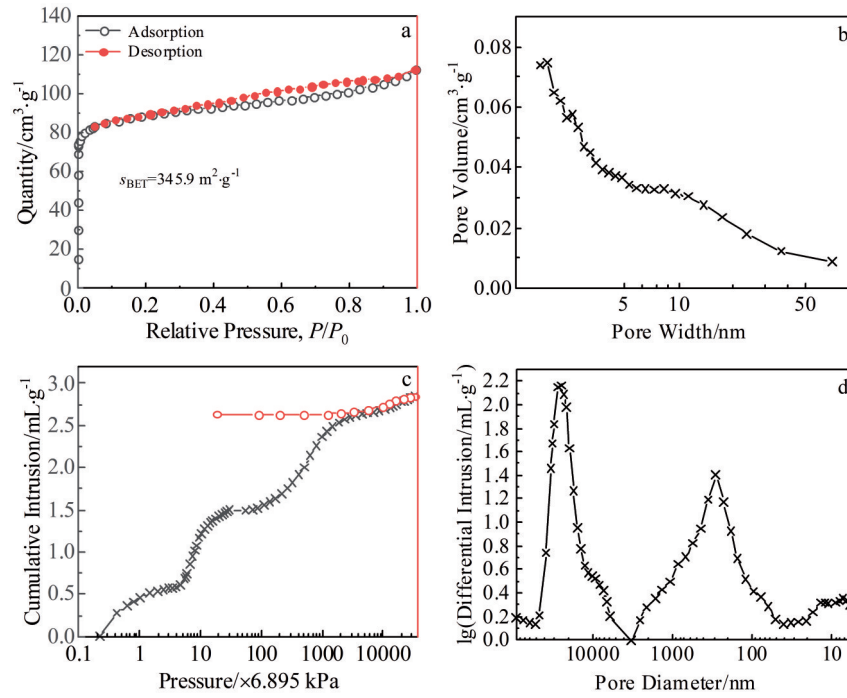


Fig.6 Nitrogen adsorption-desorption isotherms (a) and capillary pressure curve (c) of MnO-Co/biocarbon and corresponding pore distribution diagrams (b, d)

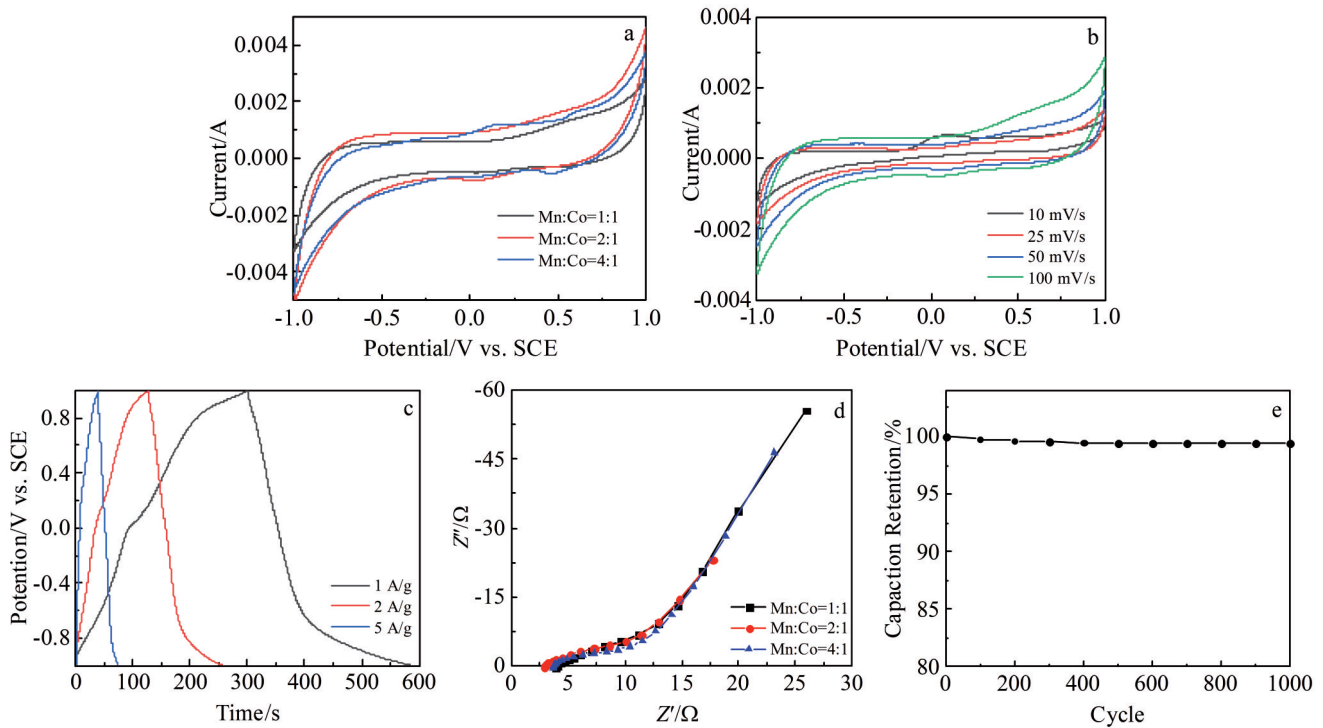


Fig.7 CV curves of MnO-Co/biocarbon with different Mn:Co ratios at the scanning rate of 100 mV/s (a); CV curves of MnO-Co/biocarbon with Mn:Co=4:1 at different scanning rates (b); charge-discharge curves of MnO-Co/biocarbon at different current densities (c); impedance Nyquist plots of MnO-Co/biocarbon with different Mn:Co ratios (d); capacitance retention of samples measured at a current density of 1 A·g<sup>-1</sup> (e)

electric double-layer capacitance and pseudocapacitance. According to the area of CV curves, the larger the ratio of Mn to Co, the greater the specific capacitance when the amount of

load is certain. Select the sample with Mn:Co=4:1 for the next test. The shape of CV curves remains unchanged (Fig. 7b), while the redox peak current increases linearly with the

increase in scanning rate from 10  $\text{mV}\cdot\text{s}^{-1}$  to 100  $\text{mV}\cdot\text{s}^{-1}$ . According to the charge-discharge test (Fig. 7c), the specific capacitance of the test sample is 146, 126.4 and 89.9  $\text{F}\cdot\text{g}^{-1}$  at 1, 2 and 5  $\text{A}\cdot\text{g}^{-1}$  current densities, respectively. It shows that the introduction of MnO-Co effectively increases its capacitance performance. When the current density increases to 2  $\text{A}\cdot\text{g}^{-1}$ , the specific capacity remains at 86.6%. When the current density increases to 5  $\text{A}\cdot\text{g}^{-1}$ , the specific capacity remains at 61.6%, showing good performance. Fig. 7d shows corresponding impedance diagram of the material. The resistance value of MnO-Co/biocrbon composites with different proportions is about 4.0  $\Omega$ , indicating that the material has good conductivity. Fig. 7e shows the specific capacitance loss measured during 1000 cycles for the sample with Mn:Co=4:1. After the whole process test, there is about 99.4% of the specific capacitance left, which means that the materials has good stability as electrode material.

### 3 Conclusions

1) MnO-Co/biocrbon composites can be prepared through a simple and low-consumption way. The large pores composed of carbon-rich layers and mesoporous accumulation of metal particles in the material and the good electron transmission ability of the biocrbon material itself provide a broad space for the loading of metal particles and the transfer of electrons.

2) Since the carbon material surface is loaded with metal composite nanocrystalline particles, the electrode material exhibits high capacitance of 146  $\text{F}\cdot\text{g}^{-1}$  at 1  $\text{A}\cdot\text{g}^{-1}$  and its energy storage efficiency can still be maintained at 99.4% after 1000 cycles.

### References

- Liu Qiang, Ye Fei, Pang Ruilvjing et al. *Materials China*[J], 2022, 41(5): 321 (in Chinese)
- Song Zhiyuan, Li Xianrong, Zhuang Changwan et al. *Rare Metal Materials and Engineering*[J], 2021, 50(10): 3485
- Zhao Jingyuan, Burke Andrew F. *Journal of Energy Chemistry*[J], 2021, 59: 276
- Kaipannan Subramani, Govindarajan Kaviarasan, Sundaramoorthy Santhoshkumar et al. *ACS Omega*[J], 2019, 4(14): 15798
- Liu Xiaoguang, Ma Changde, Li Jiabin et al. *Journal of Power Sources*[J], 2019, 412: 1
- Bommier Clement, Xu Rui, Wang Wei et al. *Nano Energy*[J], 2015, 13: 709
- Liu Bei, Liu Yijiang, Chen Hongbiao et al. *Journal of Power Sources*[J], 2017, 341: 309
- Liu Shaobo, Zhao Yang, Zhang Baihui et al. *Journal of Power Sources*[J], 2018, 381: 116
- Thirumal V, Dhamodharan K, Yuvakkumar R et al. *Chemosphere*[J], 2021, 282: 131033
- Atchudan Raji, Edison Thomas Nesakumar Jebakumar Immanuel, Perumal Suguna et al. *Chemosphere*[J], 2021, 289: 133225
- Raman Vivekanandan, Mohan N Vijay, Balakrishnan Balamuralitharan et al. *Ionics*[J], 2020, 26(1): 345
- Zhang Shun, Tian Ke, Cheng Binhai et al. *ACS Sustainable Chemistry & Engineering*[J], 2017, 5(8): 6682
- Korkmaz Satiye, Kariper I Afsin, Karaman Onur et al. *Ceramics International*[J], 2021, 47(24): 34514
- El-Deen Ahmed G, Abdel-Sattar, Mohamed K et al. *Applied Surface Science*[J], 2022, 587: 152548
- Lee Kyu Seok, Seo Ye Ji, Jeong Hyeon Taek. *Carbon Letters*[J], 2021, 31(4): 635
- Cao Yunyue, Liu Chengbao, Qian Junchao et al. *Journal of Rare Earths*[J], 2017, 35(10): 995
- Guo Yan, Yu Le, Wang Chengyang et al. *Advanced Functional Materials*[J], 2015, 25(32): 5184
- Li Liangshuo, Pang Shuhua, Fan Xin et al. *Materials Technology*[J], 2021, 37(8): 780
- Uke S J, Akhare V P, Bambole D R et al. *Frontiers in Materials*[J], 2017, 4: 21
- Wang Guoxiu, Shen Xiaoping, Horvat Josip et al. *Journal of Physical Chemistry C*[J], 2019, 113(11): 4357
- Wang Lu, Liu Xiaoheng, Wang Xin et al. *Journal of Materials Science-Materials in Electronics*[J], 2011, 22(6): 601
- Zhang Fang, Yuan Changzhou, Zhu Jiajia et al. *Advanced Functional Materials*[J], 2013, 23(31): 3909
- Cao Yunyue, Liu Chengbao, Qian Junchao et al. *Journal of Rare Earths*[J], 2017, 35(10): 995
- Moniruzzaman Md, Kumar Yedluri Anil, Pallavolu Mohan Reddy et al. *Nanomaterials*[J], 2022, 12(18): 3187
- Ramakrishnan Prakash, Shanmugam Sangaraju. *Electrochimica Acta*[J], 2014, 125: 232
- Zhang Hai, Zhang Ze, Qi Xingtao et al. *ACS Sustainable Chemistry & Engineering*[J], 2019, 7(4): 4284
- Wang Hongtao, Chen Hongtao, Hou Xin et al. *Diamond and Related Materials*[J], 2023, 136: 109888
- Liu Yurong, Zhang Jin, Hu Rong. *Ceramics International*[J], 2017, 43(5): 4427
- Radhakanth Shriram, Singhal Richa. *Chemical Engineering Science*[J], 2023, 265: 118224
- Zhang Hai, Zhang Ze, Qi Xingtao et al. *ACS Sustainable Chemistry & Engineering*[J], 2019, 7(4): 4284
- Nar Ilgin, Atsay Armagan, Altindal Ahmet et al. *Inorganic Chemistry*[J], 2018, 57(4): 2199
- Djurfors B, Broughton J N, Brett M J et al. *Acta Materialia*[J], 2005, 53(4): 957
- Phansiri Suktha, Nutthaphon Phattharasupakun, Peerapan Dittanet et al. *RSC Advances*[J], 2017, 7(16): 9958
- Wang Lianbang, Zhan Jing, Hei Jinpei et al. *Electrochimica Acta*[J], 2019, 307: 442

## 高电容电极材料 MnO-Co 纳米晶修饰多孔生物碳的简易合成

徐 杨<sup>1,2</sup>, 刘高尚<sup>1,2</sup>, 刘成宝<sup>1,2,3</sup>, 郑磊之<sup>1,2,3</sup>, 陈 丰<sup>1,2,3</sup>, 钱君超<sup>1,2,3</sup>, 邱永斌<sup>4</sup>, 孟宪荣<sup>5</sup>, 陈志刚<sup>1,2,3</sup>

(1. 苏州科技大学 江苏省环境功能材料重点实验室, 江苏 苏州 215009)

(2. 苏州科技大学 材料科学与工程学院, 江苏 苏州 215009)

(3. 苏州科技大学 江苏水处理技术与材料协同创新中心, 江苏 苏州 215009)

(4. 江苏省陶瓷研究所有限公司, 江苏 宜兴 214221)

(5. 苏州市环境科学研究所, 江苏 苏州 215007)

**摘 要:** 随着化石燃料的迅速枯竭和一系列环境问题的出现, 开发和利用新型电化学储能装置已迫在眉睫, 而电极材料的设计、制备和优化是决定超级电容器性能的关键因素。采用水热法将蜀葵秸秆转化为多孔碳基质, 并在其上锚定了 MnO 和 Co 纳米晶。结果表明, 制备的生物碳具有多孔结构和良好的电子传输特性, 而其上的纳米晶 MnO-Co 则具有高电容。由于独特的纳米碳骨架结构和较大的比表面积 ( $345.9 \text{ m}^2 \cdot \text{g}^{-1}$ ), MnO-Co 纳米晶/多孔碳显示出优异的电化学电容 ( $1 \text{ A} \cdot \text{g}^{-1}$  时为  $146 \text{ F} \cdot \text{g}^{-1}$ ) 和循环稳定性, 循环 1000 次后, 比容量仍保持在 99.4%。

**关键词:** MnO-Co 纳米晶体; 能量储存; 电极材料; 多孔生物碳

作者简介: 徐 杨, 男, 1999 年生, 硕士, 苏州科技大学材料科学与工程学院, 江苏 苏州 215009, E-mail: xuyang122596@163.com